

Multiresonant Layered Acoustic Metamaterial (MLAM) solution for broadband low-frequency noise attenuation through double-peak sound transmission loss response

D. Roca^{a,c}, J. Cante^{a,c}, O. Lloberas-Valls^{a,d}, T. Pàmies^{b,d}, J. Oliver^{a,d,*}

^a Centre Internacional de Mètodes Numèrics en Enginyeria (CIMNE)
Campus Nord UPC, Ed. C1, C/ Gran Capità s/n, 08034 Barcelona (Spain)

^b Laboratori d'Enginyeria Acústica i Mecànica (LEAM)
Campus Terrassa UPC, C/ Colom 11, 08222 Terrassa (Spain)

^c Universitat Politècnica de Catalunya (UPC), Escola Superior d'Enginyeries Industrial Aeroespacial i Audiovisuals de Terrassa (ESEIAAT)
Campus Terrassa UPC, C/ Colom 11, 08222 Terrassa (Spain)

^d Universitat Politècnica de Catalunya (UPC), Escola Tècnica Superior d'Enginyers de Camins, Canals i Ports de Barcelona (ETSECCPB)
Campus Nord UPC, Ed. C1, C/ Jordi Girona 1, 08034 Barcelona (Spain)

Abstract

The problem of noise control and attenuation is of interest in a broad range of applications, especially in the low-frequency range, below 1000 Hz. Acoustic metamaterials allow us to tackle this problem with solutions that do not necessarily rely on high amounts of mass, however most of them still present two major challenges: they rely on complex structures making them difficult to manufacture, and their attenuating capabilities are limited to narrow frequency bandwidths. Here we propose the Multiresonant Layered Acoustic Metamaterial (MLAM) concept as a novel kind of acoustic metamaterial based on coupled resonances mechanisms. Their main advantages hinge on providing enhanced sound attenuation capabilities in terms of a double-peak sound transmission loss response by means of a layered configuration suitable for large scale manufacturing.

Keywords: Acoustic Metamaterials, Coupled resonances, Layered-based panel, Sound transmission loss, MLAM

1. Motivation

For years, the notion of metamaterials has attracted the interest among the scientific community for their potential range of applications. Their attractiveness resides on the ability to exhibit customized behavior, specifically in the manipulation of waves, by engineering their internal structure. While the concept was originated in the field of electromagnetism, with metamaterials that showed both negative permittivity and permeability [24], the idea rapidly extended to other areas. In regards of the present work, the focus is on the manipulation of acoustic waves, aiming at designing a metamaterial with enhanced sound attenuation capabilities in the low-frequency region, i.e. between 100 and 1000 Hz, where most common noise sources occur (see Fig. 1).

The first notions of acoustic metamaterials emerged two decades ago, when Ping Sheng and co-workers demonstrated the concept of local resonance with a metamaterial composed of rubber-coated lead spheres, acting as internal resonators, embedded in an epoxy matrix [14]. Several other works followed, aiming at exploiting the local resonance phenomena involved in the production of frequency band gaps for improved acoustic attenuation in selected frequency regions. Beyond the early designs based on the combination of rubber-coated inclusions in a polymer matrix [4, 22, 25], examples including membranes as

internal resonators [8, 11, 27], as well as periodic arrangements of pillars on a plate [1–3], have been explored, among others. Non-periodic acoustic metamaterial configurations based on irregularities and random structures have also been studied in the past years [5, 21].

The main challenges faced by most of the proposed resonance-based acoustic metamaterials so far are: (1) the frequency bandgaps they typically produce are narrowband, and (2) they cannot be easily manufactured. The former issue is related to the local resonance phenomenon itself so it mainly affects the low frequency range (for higher frequencies, Bragg scattering effects typically produce wider bandgaps). In order to produce wider frequency bandgaps, one needs to increase the internal resonating mass in the metamaterial, which makes them lose their lightweight capabilities that makes them competitive against other classical approaches. Several works found in the literature have tried to overcome this issue, for instance, by employing multiple resonators [26, 29, 30] or combining local resonance with other damping mechanisms [10, 12, 15, 23]. However, the problem has not been entirely addressed. Multiple resonators typically lead to a collection of separated narrowband frequency bandgaps. As for the enhancements obtained through the introduction of dissipation phenomena, they are somewhat limited to very specific damping ranges (which may not be easily obtained, in practice, with conventional materials).

As for manufacturability, most of the proposed acoustic metamaterials resort to combine different material components, whose assembly presents a challenge for their practical implementa-

*Corresponding author

Email address: oliver@cimne.upc.edu (J. Oliver)

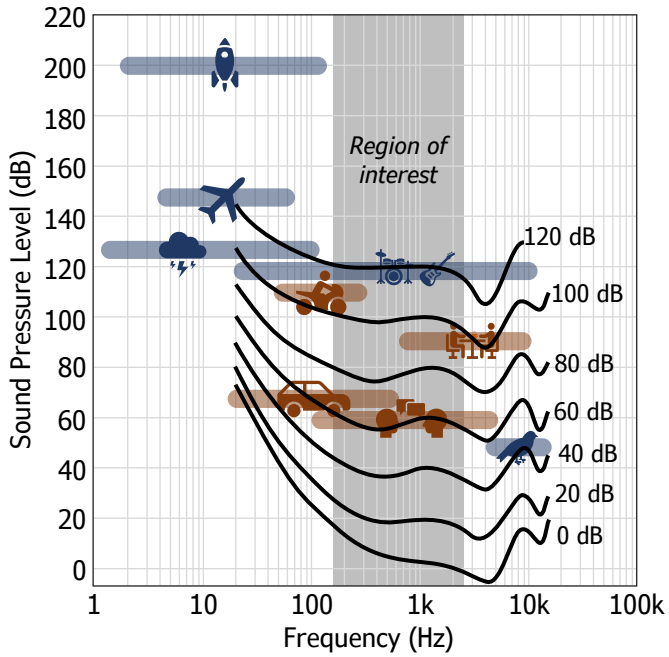


Figure 1: Sound pressure level and frequency range for common noise sources. Each solid black curve is associated to a decibel level at which each sound source is perceived by human hearing at different frequencies. As an example, traffic noise at 70 dB is perceived around this same level at frequencies in the range of 200-2000 Hz, but below 100 Hz the perceived intensity rapidly decreases, becoming practically inaudible below 30 Hz. The shaded area indicates the frequency range of interest, where most common noise sources can be found, and their perceived intensities are higher.

tion, for instance, in a mass production chain. Furthermore, ideas based on a single material component, which typically provide a solution to this problem, rely on additive manufacturing technologies due to their topological and geometrical complexity and characteristics [6, 13, 16]. This kind of technology, while presenting itself as a potential promising manufacturing option in the future, still faces many challenges nowadays, especially in terms of processing times and dimensional tolerances (see Section 4.2 for a further insight on that), which are of utmost importance in order to produce effective acoustic metamaterials in a practical manner.

As an attempt to offer a solution to these problems, a *Multiresonant Layered Acoustic Metamaterial* (MLAM) is proposed in the present work. Its constant thickness, thin layer-based configuration allows it to be easily manufactured by presently available well-known techniques. These could refer, for instance, to a process involving lamination and die cutting. While multi-layer panels based on acoustic metamaterials have been proposed in the past, they typically rely on membrane-type metamaterials in which different material components are combined in the same layer, which still represents an issue in terms of the manufacturing process (see, for instance, Refs. [17, 28]). Furthermore, in order to improve its attenuating capabilities in target frequency ranges, the internal resonances of different layers of the MLAM proposed here are coupled, which translates into an extended effective attenuation band exhibiting a double-peak

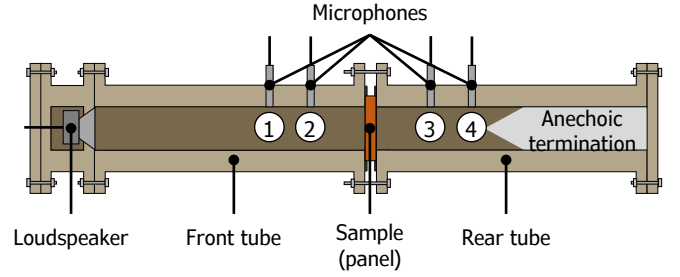


Figure 2: Experimental setting schematic representation of the two impedance tubes. The loudspeaker generates acoustic pressure plane waves on the front tube, with a fraction being reflected back by the sample panel and the remaining being transmitted through it to the rear tube. The rear tube contains an anechoic termination to avoid spurious reflections. Four microphones measure the acoustic pressure at the designated positions, which can be used to obtain the STL of the sample panel.

sound transmission loss (STL) response. The physical background behind the coupled resonances mechanism, as well as its effects in terms of the system's dispersion characteristics, is described theoretically in Gao and Wang [7] through simple spring-mass systems, but without providing an actual practical implementation. Here, we present a practical realization of the concept and analyse the consequences in terms of the STL response.

In this article, we show a methodology to numerically compute the STL response of metamaterial-based panels under normal-incidence acoustic waves. This methodology will be used to characterize the proposed MLAM attenuating capabilities, highlighting the benefits of the coupled resonances mechanism when compared to other conventional configurations. Finally, the concept will be validated through an impedance tube measurement of a 3D-printed MLAM early prototype.

2. Materials and methods

2.1. Experimental test

The experimental test considered to evaluate the performance of the prototype panel consists of an impedance tube measurement of its normal-incidence STL. This method has been used in previous works with the same purpose, to evaluate the performance of LRAM-based panels [20]. Since a detailed description of the whole methodology can be found in Roca et al. [20], here we will focus only on the most relevant aspects of it.

The impedance tube setup (depicted in Fig. 2) consists of two tube parts with the same constant inner section. On one end of the front tube, a loudspeaker (VISATON FRS 8-4 Ohm, with a nominal diameter of 8 cm, 30 W, and linear frequency response from 200 and 20000 Hz) connected to a six channel amplifier (ECLER MPA 6-80) emits a pink noise (noise source on the whole audible frequency spectrum with equal amount of energy for each octave). The last 30 cm on the opposite end of the rear tube are filled with a polyurethane foam acting as an anechoic termination. The sample panel is placed between the two tubes, pressed against a soft sealing material that prevents

sound from leaking while not fully restricting the panel's motion on the longitudinal direction. This particular setting deviates from the standard method described in ASTM E1050-98, where the sample typically fills the inside of the tubes' section. However, it allows more flexibility in the sample's shape while still proving to capture local resonance mechanisms on metamaterial-based panel configurations [9, 20]. Finally, two pairs of 0.5 in. prepolarized microphones (electret condenser model GRAS 40AE) with an integrated circuit piezoelectric (ICP) preamplifier (model GRAS 26CA) are located at different tube positions. They measure the acoustic pressure at these points, from which the STL can be computed. The tubes' section size of 8 cm \times 8 cm and the separation distance between each pair of microphones of 7.6 cm guarantee an applicability range between 200 and 2000 Hz for normal-incidence acoustic plane waves.

The procedure to compute the STL starts with the measured pressure values at the four microphone positions, which can be written in the frequency domain as

$$P_1(\omega) = A(\omega)e^{i\kappa x_1} + B(\omega)e^{-i\kappa x_1}, \quad x_1 = -17.6 \text{ cm}; \quad (1)$$

$$P_2(\omega) = A(\omega)e^{i\kappa x_2} + B(\omega)e^{-i\kappa x_2}, \quad x_2 = -10 \text{ cm}; \quad (2)$$

$$P_3(\omega) = C(\omega)e^{i\kappa x_3} + D(\omega)e^{-i\kappa x_3}, \quad x_3 = d + 10 \text{ cm}; \quad (3)$$

$$P_4(\omega) = C(\omega)e^{i\kappa x_4} + D(\omega)e^{-i\kappa x_4}, \quad x_4 = d + 17.6 \text{ cm}, \quad (4)$$

where A and B are the complex pressure amplitudes of the incidence and reflected waves on the front tube, respectively, C and D are the complex pressure amplitudes of the transmitted and reflected waves on the rear tube, respectively, d is the panel's thickness, and κ is the wavenumber, defined as

$$\kappa = \frac{\omega}{c}, \quad (5)$$

with ω being the frequency and c the speed of sound in air. Each x_k in the Eqs. (1)-(4) refers to the relative position of the k -th microphone with respect to the panel's incidence surface.

The anechoic termination condition allows us to neglect the effect of the reflected wave on the rear tube (i.e., $D = 0$), thus the transmission coefficient T of the sample panel can be obtained simply as

$$T(\omega) = \frac{C(\omega)}{A(\omega)}, \quad (6)$$

where A and C are computed according to:

$$A(\omega) = i \frac{\bar{P}_1 e^{-i\kappa x_2} - \bar{P}_2 e^{-i\kappa x_1}}{2 \sin \kappa(x_2 - x_1)}, \quad (7)$$

$$C(\omega) = i \frac{\bar{P}_3 e^{-i\kappa x_3} - \bar{P}_4 e^{-i\kappa x_4}}{2 \sin \kappa(x_4 - x_3)}. \quad (8)$$

with \bar{P}_k being the calibrated complex Fourier transformed pressure measured for the k -th microphone. The calibration process to correct the amplitude and phase of the pressure amplitudes follows the standard ASTM E1050-98 and is described also in Roca et al. [20].

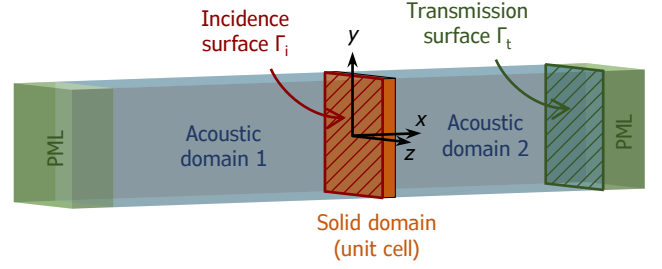


Figure 3: Schematic representation of the problem setting for numerically computing the STL of a panel with a periodically repeating unit cell. Two perfectly matched layers (PML) are considered at the ends of the acoustic domains to simulate an infinite extension of the domain in all directions. The STL is obtained by computing the average amplitude of the incidence and transmitted pressure fields on the designated surfaces Γ_i and Γ_t , respectively.

The STL can finally be obtained by inserting Eqs. (7) and (8) into Eq. (6) and using the formula:

$$\text{STL}(\omega) = -10 \log_{10} |T|^2. \quad (9)$$

2.2. Numerical simulations

The objective of the numerical simulations here is to compute the STL of an acoustic metamaterial panel characterized by a unit cell that infinitely repeats in the transverse directions. To properly account for this STL parameter, the acoustic domains (filled with air, where acoustic pressure plane waves propagate), must be also infinite on each side of the solid panel. To perform such analysis, the schematic representation in Fig. 3 is considered. The domain is split into an acoustic domain (the air), where the pressure field is the primary unknown, and a solid domain (the metamaterial panel), where the displacement field is the primary unknown.

(a) Acoustic domain:

In the acoustic domain, the pressure field is solved in terms of the frequency, ω , from the Helmholtz equation

$$\nabla^2 p_t + \kappa^2 p_t = 0, \quad (10)$$

where κ is the wavenumber, as previously defined in Eq. (5), and

$$p_t = p_s + p_b \quad (11)$$

is the total pressure field, defined as the sum of the scattered pressure field, p_s (the actual unknown), and the background pressure field, p_b .

To simulate a normal-incidence acoustic plane wave, the background pressure field in the acoustic domain 1 (the incidence side) is imposed to

$$p_b = p_0 e^{-i\kappa x}, \quad \forall x < 0 \quad (12)$$

where $p_0 = 0.02$ Pa (this value corresponds to a sound pressure

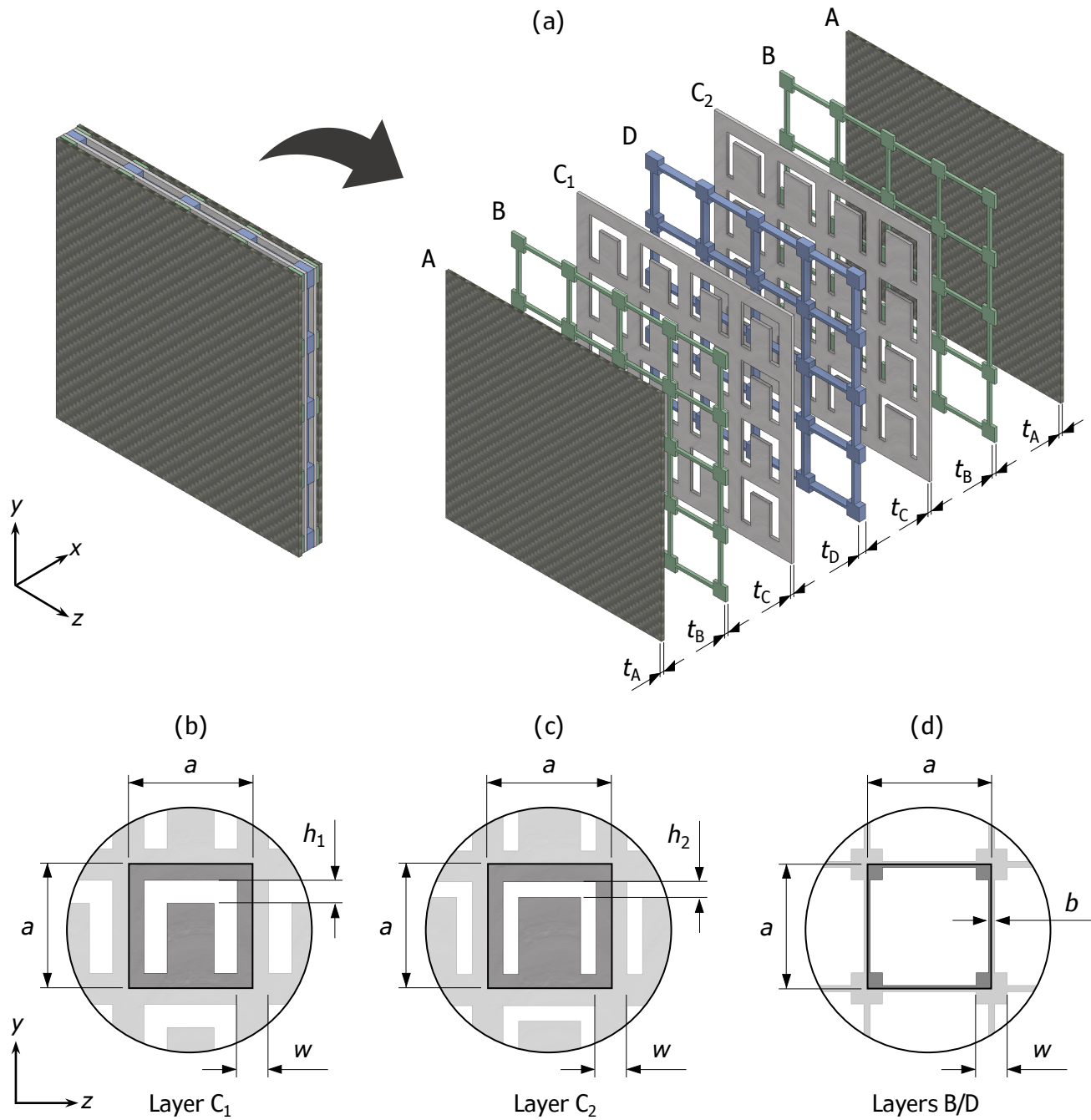


Figure 4: (a) Representation of the MLAM layered structure with an example of its different types of layers. (b) Detailed geometrical parameters and structure of the U-shaped unit cell in the first resonating layer (C₁). (c) Detailed geometrical parameters and structure of the U-shaped unit cell in the second resonating layer (C₂). (d) Detailed geometrical parameters and structure of the unit cell in the the separating and connecting layers (B and D).

level of 60 dB, but is taken simply as a reference, since it does not affect the resulting STL). In the acoustic domain 2 (transmission side), $p_b = 0$.

At both ends of the acoustic domain (in the x -direction), perfectly matched layers (PMLs) are imposed to avoid wave reflections, hence simulating the medium's infinite extension.

(b) *Solid domain:*

In the solid domain, the displacement field, \mathbf{u} , is solved from the momentum balance equation in the frequency domain,

$$\nabla \cdot \boldsymbol{\sigma} + \rho \omega^2 \mathbf{u} = \mathbf{0}, \quad (13)$$

where ρ is the material's density field and $\boldsymbol{\sigma}$ is the stress tensor field. In this context, small displacements and strains can be assumed, so a linear elastic material model is considered. In particular,

$$\boldsymbol{\sigma} = \mathbb{C} : \nabla^S \mathbf{u}, \quad (14)$$

where ∇^S denotes the symmetric gradient operator and \mathbb{C} is the fourth-order constitutive tensor, which can be expressed, using Voigt's notation, in terms of the material's Young's modulus, E , and Poisson's ratio, ν , as

$$\mathbb{C}^{\text{Voigt}} = \begin{bmatrix} \lambda + 2\mu & \lambda & \lambda & 0 & 0 & 0 \\ \lambda & \lambda + 2\mu & \lambda & 0 & 0 & 0 \\ \lambda & \lambda & \lambda + 2\mu & 0 & 0 & 0 \\ 0 & 0 & 0 & \mu & 0 & 0 \\ 0 & 0 & 0 & 0 & \mu & 0 \\ 0 & 0 & 0 & 0 & 0 & \mu \end{bmatrix}, \quad (15)$$

$$\text{with } \lambda = \frac{\nu E(1 + i\eta)}{(1 + \nu)(1 - 2\nu)}, \quad \mu = \frac{E(1 + i\eta)}{2(1 + \nu)},$$

where η is used here as an isotropic loss factor to account for damping in the system (notice that i refers to the imaginary number, so the tensor \mathbb{C} becomes complex valued for $\eta \neq 0$). It should be remarked that damping does not play a major role into the expected material behaviour (it is introduced simply to characterize a more realistic response), so this simple model provides just a measure of each material's dissipation capacity, regardless of the specific sources (it takes into account, for instance, visco-elastic or thermo-viscous effects).

(c) *Acoustic-structure interface:*

On the boundaries between the solid and acoustic domains, the effect of the pressure field on the solid domain is accounted for as an external traction force

$$\boldsymbol{\sigma} \cdot \mathbf{n} = -p_t \mathbf{n}, \quad (16)$$

where \mathbf{n} is the outward unit vector of the solid's boundary surface. Additionally, compatibility of the normal component of

the displacements is considered through

$$\mathbf{n} \cdot \nabla p_t = \omega^2 \rho_a \mathbf{u} \cdot \mathbf{n}, \quad (17)$$

where ρ_a is the air's density.

(d) *Periodic boundary conditions:*

Given the periodic configuration of the acoustic metamaterial structure, the analysis is focused on a single unit cell while still accounting for the infinite transverse extension of the panel. In general, this is achieved through imposing Floquet boundary conditions in the y and z -directions, both on the solid and the acoustic domains:

$$p_t(\mathbf{x}^{(+)}) = p_t(\mathbf{x}^{(-)}) e^{i\mathbf{k} \cdot (\mathbf{x}^{(+)} - \mathbf{x}^{(-)})} \quad (18)$$

$$\mathbf{u}(\mathbf{x}^{(+)}) = \mathbf{u}(\mathbf{x}^{(-)}) e^{i\mathbf{k} \cdot (\mathbf{x}^{(+)} - \mathbf{x}^{(-)})} \quad (19)$$

where $\mathbf{x}^{(-)}$ and $\mathbf{x}^{(+)}$ refer to the source and corresponding destination points, respectively, of the periodic boundaries.

For this particular case, in which we consider waves propagating in the x -direction (normal-incidence, i.e. $\kappa_y = \kappa_z = 0$), conditions expressed by Eqs. (18) and (19) turn into standard periodic boundary conditions.

(e) *STL computation:*

Equations (10) and (13) are solved considering a FEM discretization using the standard coupled acoustic-solid model in COMSOL. Once the pressure and displacement fields are obtained, for a given frequency, the corresponding STL is computed as in Eq. (9), with the transmission coefficient, T , obtained through

$$T = \frac{\int_{\Gamma_t} p_t d\Gamma}{\int_{\Gamma_i} p_b d\Gamma}, \quad (20)$$

where Γ_i and Γ_t denote the incidence and transmission surfaces, respectively, as depicted in Fig. 3.

3. Proposed design

The MLAM design concept is based on a stack of *constant thickness* layers of *homogeneous materials*. Each of these layers is characterized by its specific material properties, thickness and unit cell's design/topology (see Fig. 4(a)). In order to operate properly (i.e., exhibit the coupled resonances and the double-peak effects), different layers with particular purposes are required:

- a) *Resonating layers* (e.g. layers C_i in Fig. 4(a)). They represent the core layers of the MLAM structure, as they contain the resonating elements responsible for triggering local resonance effects, causing the STL attenuation peaks. In this kind of layers, the unit cell's topology and dimensions play an important role in determining the location of these peaks on the frequency spectrum. The

Material	Density ρ (kg/m ³)	Young's modulus E (MPa)	Poisson's ratio ν	Loss factor η	Layers
Polyamide (PA)	1050	1650	0.4	0.005	A, B
Steel	7800	200000	0.3	0	C ₁ , C ₂
Silicone rubber	1050	0.15	0.47	0.02	D
Parameter	MLAM	UMLAM	SLAM	HP	HP+
t_A (mm)	1 / 1	1 / 1	2.9 / 2.9	9.5	38
t_B (mm)	0.5 / 0.5	0.5 / 4 / 0.5	1 / 1	-	-
t_{C_1} (mm)	0.75	0.75	0.75	-	-
t_{C_2} (mm)	0.75	0.75	-	-	-
t_D (mm)	4	-	-	-	-
a (mm)	40	40	40	-	-
b (mm)	1	1	1	-	-
w (mm)	4	4	4	-	-
h_1 (mm)	8	8	6	-	-
h_2 (mm)	4	4	-	-	-
Total thickness (mm)	8.5	8.5	8.55	9.5	38
Surface density (kg/m ²)	9.96	9.96	9.95	9.98	39.9

Table 1: Material properties and geometrical parameters considered for obtaining the STL curves in Fig. 5. Each material is assigned to the corresponding layer types (as defined in Fig. 4) indicated in the layers column. The definition of all the geometric parameters can also be found in Fig. 4. The last two rows in the table provide detailed information regarding each panel configuration's total thickness and surface density, respectively.

simple “U-shaped” design considered for the proposed prototype (see Fig. 4(b)-(c)) is enough to guarantee a good STL response in the frequency range below 1 kHz. In this case, the overall performance of the STL is improved when choosing denser materials for the resonating layers, since it allows them to be more compact and thin.

- b) *Connecting layers* (e.g. layer D in Fig. 4(a)). As the name suggests, the purpose of these layers is to connect pairs of resonating layers, and so they must be stacked between them as depicted in Fig. 4(a). Their presence in the MLAM structure is key to enable the coupling resonances effects. In this case, their associated unit cells' pattern must be compatible with that of the resonating layers', making sure the corresponding unit cells' boundaries match (see Fig. 4(c)). The specific dimensions and material choice for this kind of layers is also important to guarantee a good coupling effect. This can be adjusted through the effective stiffness of the layer. If the connecting layer is too stiff, the resonating layers become effectively uncoupled and the corresponding STL attenuation peaks wouldn't be connected (see Fig. 5). Thus, softer (rubber-like) materials would be preferred in this case to guarantee the coupling with a more compact and thin configuration.
- c) *Separating layers* (e.g. layers B in Fig. 4(a)). These layers are adjacent to resonating layers since their whole purpose is to enable the vibration of their resonating elements. For this reason, their unit cells' pattern must again be compatible with that of the resonating layers. To cause minimal interference with the overall performance of the MLAM structure, these layers should be ideally thin and stiff enough to isolate each unit cell's vibration from the

others (otherwise, it can cause undesired effects on their associated local resonances due to triggering unit cell's deformation modes in the frequency range of interest).

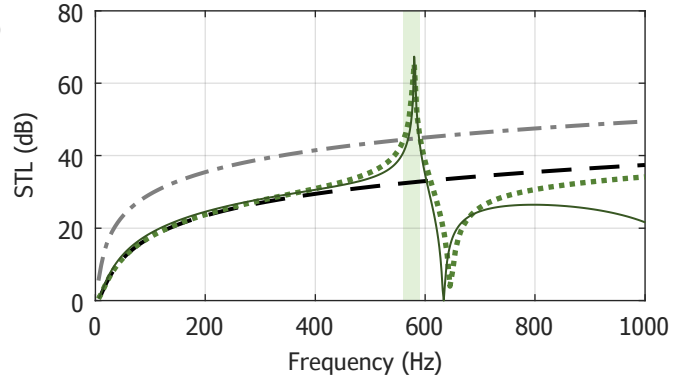
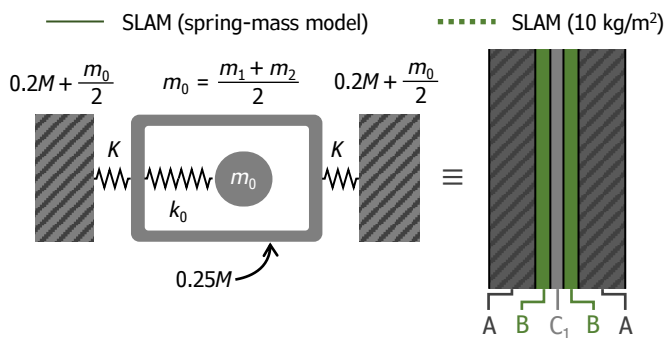
- d) *Skin layers* (e.g. layers A in Fig. 4(a)). These layers are homogeneous solid covers (with no associated unit cell pattern), present for supporting the whole stack, and also for protection purposes. Since they do not play a major role in the MLAM performance, they should have enough stiffness to avoid interference with the STL response. For some applications in which the MLAM panel is attached to some structure (e.g. a wall), the corresponding skin layer could be removed (hence attaching the separating layer directly onto the structure) while still exhibiting the relevant effects on the STL response.

4. Results

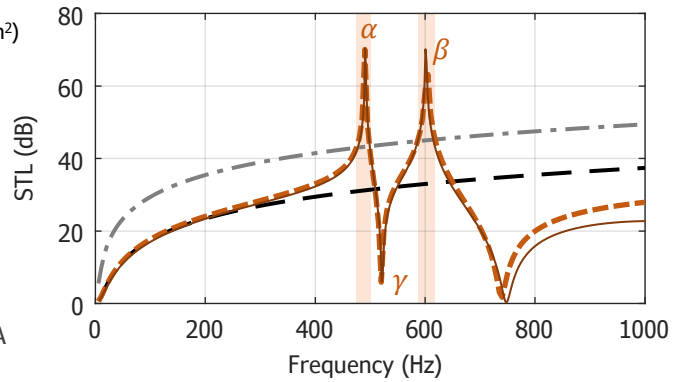
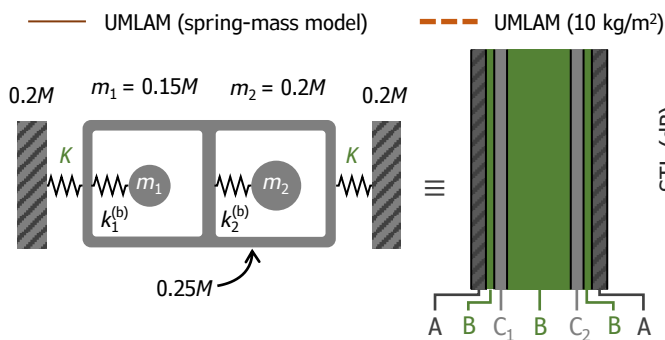
4.1. Double-peak STL response

In Fig. 5, we show the STL response of three different layered-based acoustic metamaterial configurations: (a) one with a single resonating layer (SLAM), (b) another with two uncoupled resonating layers (UMLAM), and (c) the MLAM concept (i.e., with two coupled resonating layers). For each case, Fig. 5 shows the equivalent spring-mass systems: (a) a mass-in-mass configuration describing a conventional acoustic metamaterial, (b) two different inner masses inside the same outer mass (i.e., an acoustic metamaterial with two internal resonators), and (c) two different mass-in-mass units contained in the same supercell structure (i.e., two coupled acoustic metamaterial units). The general idea behind the MLAM realization of its equivalent spring-mass system (c) is that the cells represent the corresponding resonating layers (C₁ and C₂), the masses at each end are

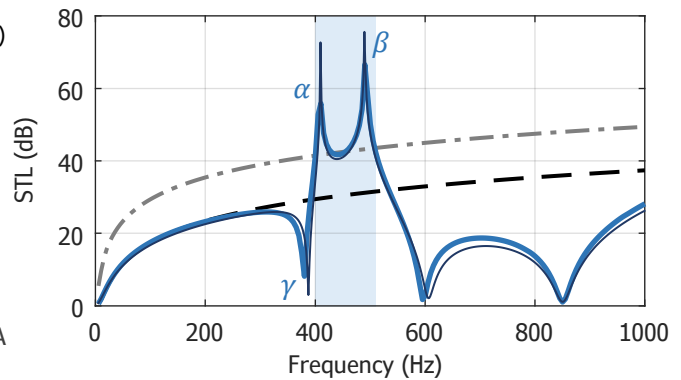
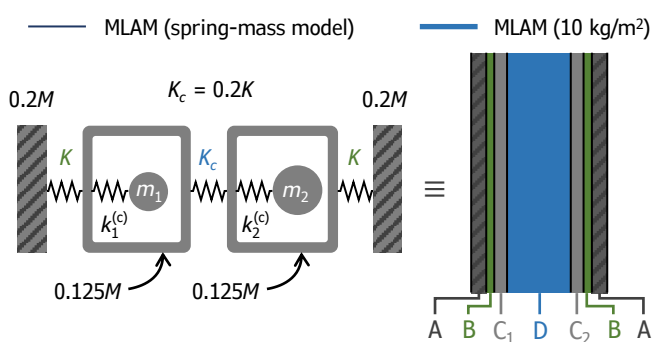
(a) Single resonator acoustic metamaterial (SLAM)



(b) Uncoupled two-resonator acoustic metamaterial (UMLAM)



(c) Coupled two-resonator acoustic metamaterial (MLAM)



— — — Homogeneous panel, HP (10 kg/m²) - - - - Homogeneous panel, HP+ (40 kg/m²)

Figure 5: On the left, the three different layered-based acoustic metamaterial configurations are depicted, with their respective layer types composition, along with an equivalent spring-mass system representation. On the right, the corresponding STL curves for each case are shown and compared to the results for homogeneous panels of the same surface density (10 kg/m²) and four times that (40 kg/m²). The shaded areas in the plots correspond to frequency regions in which the metamaterial configurations exhibit levels of attenuation higher than those obtained with comparable homogeneous panels with four times more mass. For reference, the thin continuous lines on the right plots represent the STL curves for each equivalent spring-mass system.

Materials (3D-printing)		Density ρ (kg/m ³)	Young's modulus E (MPa)	Poisson's ratio ν	Layers				
Polyamide (PA)		1010	1800	0.4	A, B				
Steel		7860	147000	0.3	C ₁ , C ₂				
Rubber-like		1200	85	0.48	D				
t_A (mm)	t_B (mm)	t_{C_1} (mm)	t_{C_2} (mm)	t_D (mm)	a (mm)	b (mm)	w (mm)	h_1 (mm)	h_2 (mm)
2 / 2	1 / 1	2	2	15	40	1	10	3	8

Table 2: Material properties and geometrical parameters for the MLAM prototype used in the experiments and the corresponding numerical simulations. Each material is assigned to the corresponding layer types (as defined in Fig. 4) indicated in the layers column. The definition of all the geometric parameters can also be found in Fig. 4. The material properties are obtained from the datasheets of the manufacturer.

assumed as the skin layers (A), and the roles of springs K and K_c are taken by the separating layers (B) and connecting layer (D), respectively. Analogous considerations can be assumed for the spring-mass systems (a) and (b) with the SLAM and UMLAM configurations, respectively.

The material properties and geometric characteristics of each panel configuration are detailed in Tab. 1. For comparative purposes, all three acoustic metamaterial panels have almost the same total thickness and mass. Notice that the only difference between the UMLAM and the MLAM is the material choice for the layer between the two resonating layers. For the uncoupled configuration (UMLAM), the same polymer-like material of the separating layers (type B layers) is considered, while a softer rubber-like material (with the same density) is chosen for the MLAM case, making it a truly connecting layer (type D layer), and hence exhibiting the coupled resonances effect and the double-peak STL response. In the SLAM configuration, the skin and separating layers' thicknesses have been increased to match the global mass and thickness of the other two configurations. To properly analyse the STL response, the obtained curves for each case in Fig. 5 are compared with the corresponding results for reference homogeneous panel (HP) configurations of the same surface density (of 10 kg/m²) and 4 times that (40 kg/m², named HP+). As an example, these could refer to steel panels of 1.28 mm and 5.12 mm thick, respectively, or polyamide (PA) panels of 9.5 mm and 38 mm thick (considering the densities provided in Tab. 1).

Additionally, to support the physical insight provided by the equivalent spring-mass systems, the STL plots in Fig. 5 also show their corresponding STL curves. To obtain these results, the conditions of incident, reflected and transmitted plane waves have been imposed in terms of non-dimensional displacements and forces acting on the end masses:

$$\hat{u}_L = (1 - R)e^{i\omega t}, \quad \hat{u}_R = T e^{i\omega t}; \quad (21)$$

$$\hat{f}_L = i\hat{\omega}\gamma(1 + R)e^{i\omega t}, \quad \hat{f}_R = -i\hat{\omega}\gamma T e^{i\omega t}. \quad (22)$$

Here, the subscripts ‘‘L’’ and ‘‘R’’ refer to the ‘‘left’’ and ‘‘right’’ end masses, respectively. Variables R and T are the reflection and transmission coefficients, $\hat{\omega} = \omega/\Omega_0$ (with $\Omega_0^2 = K/M$), and $\gamma = \dot{m}_{\text{air}}/M\Omega_0$ (with $\dot{m}_{\text{air}} \sim \rho_{\text{air}}c_{\text{air}}$ being a reference air mass flow rate). While no straightforward (direct) association between the springs and masses can be made with the corresponding 3D realization parameters, both systems can be made

equivalent (in terms of their STL response) with an appropriate choice of the variables $\gamma = 0.008$ and $\Omega_0 = 600$ Hz, along with the total mass M distribution detailed in Fig. 5 (this selection of parameters comes from attempting to fit the spring-mass model results to those for its corresponding 3D implementation). In this case, the values considered for k_0 , $k_i^{(b)}$ and $k_i^{(c)}$ ($i = 1, 2$), defined in Fig. 5, come from matching the frequencies of their corresponding resonance STL peaks. Notice that, for the MLAM case, a lower stiffness for the connecting spring, $K_c = 0.2K$, has been required to achieve the resonance coupling effect.

As expected, the more conventional acoustic metamaterial configuration, i.e. consisting of a single resonator/unit cell design, produces an STL response characterized by an attenuation peak followed by a transmission dip on frequencies that, for plane waves at normal incidence, coincide with the associated bandgap limits [18, 19] (see Fig. 5(a)). The idea of exploiting the local resonance effects of different resonators can be conceived as a way to obtain higher levels of attenuation in an extended frequency range. However, the use of multiple resonators is not enough to guarantee a broader range of attenuation in the panel's STL response. To properly exploit them, the resonators also need to be coupled, otherwise they will produce several narrowband attenuation peaks isolated from one another (i.e., with transmission dips in-between). Through the resonators' coupling, their locally resonant bandgaps are joined into a continuous larger gap (translating into the double-peak STL response). This can be appreciated comparing the STL responses in Figs. 5(b) and 5(c).

Notice that through the resonating layers' coupling, one effectively makes the transmission dip that typically appears *after* the STL peaks produced by local resonances (see γ in Fig. 5(b) appearing between peaks α and β), to occur *before* the first attenuation peak (see now γ appearing before peaks α and β in Fig. 5(c)), creating an extended single, continuous attenuation band between the two attenuation peaks. When comparing the results with those of a homogeneous panel 4 times heavier, the MLAM configuration clearly shows how we can get the same effective attenuation levels in the whole range between 400 Hz and 500 Hz. In both other cases, the comparative STL levels are only achieved in very narrow, isolated frequency bands (of less than 30 Hz). It is also worth noting that this enhanced STL response occurs at lower frequencies for the MLAM configuration compared to the equivalent single resonator and two un-

coupled resonators cases, which is an additional advantage.

4.2. Experimental validation

In order to validate the MLAM concept experimentally, a 3D-printed prototype of the configuration depicted in Fig. 4 was tested following the procedure described in Section 2.1. The material properties and geometrical parameters for this case are given in Tab. 2. It should be noticed that, at present, there are limited options in terms of materials available for the 3D-printing technology and, in most cases, there are additional design constraints that need to be taken into account. For instance, the minimum thickness of the layers. Furthermore, since silicone rubber was not available as a material choice for the connecting layer, the closest alternative was a powder-based material that, in its final form (achieved through a Multi-Jet Fusion process), it exhibits some rubber-like behaviour. While being certainly softer than most conventionally polymer-based materials, this material’s stiffness is still 1-2 orders of magnitude higher than that of common silicone rubber materials, which required a noticeable increase of the connecting layer’s thickness to compensate, and make the coupled resonances work. Once each different layer component was 3D-printed, they were glued together forming a MLAM stack. The tackled frequency range of attenuation for the prototype is around 1000 Hz (in contrast to the 400-500 Hz range considered in Fig. 5 numerical simulations) due to the material options and geometric tolerances for the available manufacturing process.

Four different tests were performed on the same prototype, with Fig. 6 showing the average of the obtained results. The results show more than 20 dB increase over a range of 200 Hz between two clearly defined peaks at 1000 Hz and 1100 Hz. These experimental results are consistent with the expected STL curves obtained from the numerical simulation, especially when considering an appropriate amount of damping, with a loss factor of $\eta = 0.02$ (expressly chosen to match to the experimental results). The experiment setting does not reproduce the ideal conditions of the numerical simulations, which explains some of the differences between both curves (like, for instance, the appearance of small spurious peaks between 800 and 900 Hz). The lower STL level achieved in the experimental test for lower frequencies (minus 10 dB compared to the simulation results) is likely due to small sound leaks, caused by a non-perfect isolation inside the tube and to the particular sample holding approach. Finally, dimensional tolerances during the manufacturing process (and possible inaccuracies in the material properties provided by the manufacturer that have been used in the simulations) may be cause of small frequency shifts in the expected STL peaks. Despite these small discrepancies the experimental results clearly show the expected enhanced STL response, with an extended effective attenuation band due to two joined STL peaks in the predicted frequency range.

5. Conclusions

Results for the MLAM design proposed show great potential for it to become a practical lightweight, sound attenuating

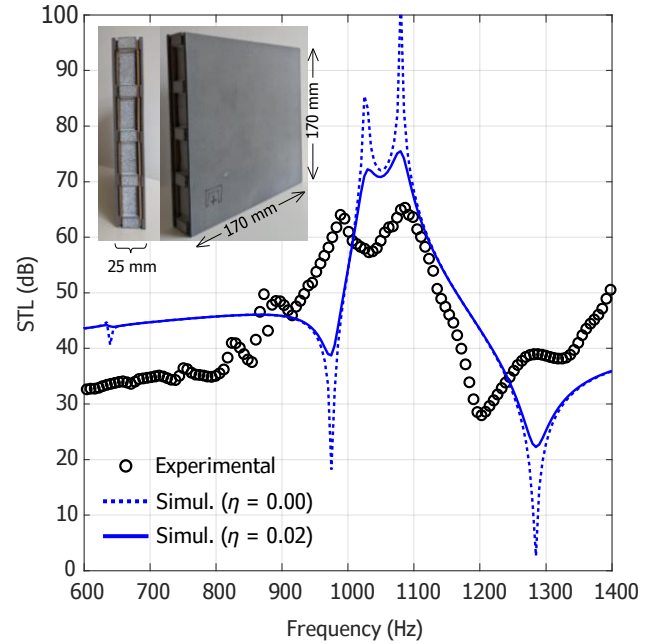


Figure 6: Sound transmission loss curve, obtained experimentally for the MLAM prototype, compared to the corresponding numerical simulation results for $\eta = 0$ (no damping) and $\eta = 0.02$. The inset on the top left depicts a side view and a front view of the actual 3D-printed prototype employed with the whole panel dimensions (detailed layer composition, including geometrical parameters and materials, are given in Tab. 2).

solution at lower frequency ranges. Its main advantage over other conventional acoustic metamaterial configurations stems from its layer-based structure, that makes it suitable for large-scale production through well-established manufacturing processes. Additionally, by taking advantage of the coupled resonances phenomenon combined with the acoustic metamaterials’ local resonance effects, it manages to produce STL responses exhibiting wider effective attenuation bands at lower frequencies, compared to equivalent single-resonator or uncoupled multi-resonator based acoustic metamaterials.

While the proposed designs in the present work provide a first notion of what are the capabilities of the MLAM technology, along with its validation through an early 3D-printed prototype, there are still issues to tackle. Early studies suggest that there is a compromise between extending the attenuation bandwidth (by separating the resonance frequencies) and the STL level achieved. This affects also the coupling mechanism, which is not triggered when these resonances are separated beyond a certain value. For the samples presented in Fig. 4, attenuation bandwidths of up to 200 Hz can still be achieved, but with significantly lower STL performances. However, this limit is linked to material and geometrical features of the MLAM design, and a more detailed analysis would be a topic for future research. In this regard, exploring the effects of coupling several MLAM panels or investigating the role of the layers’ design and topology into optimizing the STL response could lead to more efficient performances (either by increasing the attenuation level or further extending the effective attenuation

band). Also, it would be interesting to perform experimental tests on prototypes produced with more suitable manufacturing techniques (for instance, lamination combined with die cutting) to analyze possible challenges and limitations of the technology that would be considered in future, more optimized MLAM designs.

Acknowledgements

This research has received funding from the European Research Council (ERC) under the European Union’s Horizon 2020 research and innovation program (Proof of Concept Grant call reference ERC-2019-PoC-25-04-2019, Proposal No. 874481) through the project “Computational design and prototyping of acoustic metamaterials for tailored insulation of noise” (META-COUSTIC). The authors also acknowledge the financial support received by the Spanish Ministry of Economy and Competitiveness, through the Research Grant DPI2017-85521-P for the project “Computational Design of Acoustic and Mechanical Metamaterials” (METAMAT) and the “Severo Ochoa Programme for Centres of Excellence in R&D” (CEX2018-000797-S). The authors would like to acknowledge Prof. Mahmoud Hussein, for the insights behind the physics of the coupled resonances mechanism. Finally, the authors would like to gratefully acknowledge Dr. Jordi Romeu and the LEAM group for facilitating the realization of the experimental part of this work.

References

- [1] M. Badreddine Assouar and Mourad Oudich. Enlargement of a locally resonant sonic band gap by using double-sides stubbed phononic plates. *Applied Physics Letters*, 100(12):123506, mar 2012. ISSN 0003-6951. doi: 10.1063/1.3696050.
- [2] M. Badreddine Assouar, Matteo Senesi, Mourad Oudich, Massimo Ruzzene, and Zhilin Hou. Broadband plate-type acoustic metamaterial for low-frequency sound attenuation. *Applied Physics Letters*, 101(17):173505, oct 2012. ISSN 0003-6951. doi: 10.1063/1.4764072.
- [3] Osama R Bilal, André Foehr, and Chiara Daraio. Observation of trampoline phenomena in 3D-printed metamaterial plates. *Extreme Mechanics Letters*, 15:103–107, sep 2017. ISSN 23524316. doi: 10.1016/j.eml.2017.06.004.
- [4] Emilio P. Calius, Xavier Bremaud, Bryan Smith, and Andrew Hall. Negative mass sound shielding structures: Early results. *physica status solidi (b)*, 246(9):2089–2097, sep 2009. ISSN 03701972. doi: 10.1002/pssb.200982040.
- [5] Paolo Celli, Behrooz Yousefzadeh, Chiara Daraio, and Stefano Gonella. Bandgap widening by disorder in rainbow metamaterials. *Applied Physics Letters*, 114(9):091903, mar 2019. ISSN 0003-6951. doi: 10.1063/1.5081916.
- [6] Claus Claeys, Elke Deckers, Bert Pluymers, and Wim Desmet. A lightweight vibro-acoustic metamaterial demonstrator: Numerical and experimental investigation. *Mechanical Systems and Signal Processing*, 70-71:853–880, mar 2016. ISSN 08883270. doi: 10.1016/j.ymsp.2015.08.029.
- [7] Yuqiang Gao and Lifeng Wang. Ultrawide coupled bandgap in hybrid periodic system with multiple resonators. *Journal of Applied Physics*, 127(20):204901, may 2020. ISSN 0021-8979. doi: 10.1063/1.5142066.
- [8] Morgan Hiraiwa, M. Abi Ghanem, S. P. Wallen, Amey Khanolkar, A. A. Maznev, and Nicholas Boechler. Complex Contact-Based Dynamics of Microsphere Monolayers Revealed by Resonant Attenuation of Surface Acoustic Waves. *Physical Review Letters*, 116(19):198001, may 2016. ISSN 0031-9007. doi: 10.1103/PhysRevLett.116.198001.
- [9] Kin Ming Ho, Z. Yang, X.X. Zhang, and Ping Sheng. Measurements of sound transmission through panels of locally resonant materials between impedance tubes. *Applied Acoustics*, 66(7):751–765, jul 2005. ISSN 0003682X. doi: 10.1016/j.apacoust.2004.11.005.
- [10] Mahmoud I. Hussein and Michael J. Frazier. Metadamping: An emergent phenomenon in dissipative metamaterials. *Journal of Sound and Vibration*, 332(20):4767–4774, sep 2013. ISSN 0022460X. doi: 10.1016/j.jsv.2013.04.041.
- [11] Amey Khanolkar, Samuel Wallen, Maroun Abi Ghanem, Jennifer Jenks, Nicolas Vogel, and Nicholas Boechler. A self-assembled metamaterial for Lamb waves. *Applied Physics Letters*, 107(7):071903, aug 2015. ISSN 0003-6951. doi: 10.1063/1.4928564.
- [12] A.O. Krushynska, V.G. Kouznetsova, and M.G.D. Geers. Visco-elastic effects on wave dispersion in three-phase acoustic metamaterials. *Journal of the Mechanics and Physics of Solids*, 96:29–47, nov 2016. ISSN 00225096. doi: 10.1016/j.jmps.2016.07.001.
- [13] Alexandre Leblanc and Antoine Lavie. Three-dimensional-printed membrane-type acoustic metamaterial for low frequency sound attenuation. *The Journal of the Acoustical Society of America*, 141(6):EL538–EL542, jun 2017. ISSN 0001-4966. doi: 10.1121/1.4984623.
- [14] Z. Liu, X. Zhang, Y. Mao, Y. Zhu, Z. Yang, C. T. Chan, and P. Sheng. Locally Resonant Sonic Materials. *Science*, 289(5485):1734–1736, sep 2000. ISSN 00368075. doi: 10.1126/science.289.5485.1734.
- [15] James M. Manimala and C. T. Sun. Microstructural design studies for locally dissipative acoustic metamaterials. *Journal of Applied Physics*, 115(2):023518, jan 2014. ISSN 0021-8979. doi: 10.1063/1.4861632.
- [16] Olivia McGee, Huan Jiang, Feng Qian, Zian Jia, Lifeng Wang, Han Meng, Dimitrios Chronopoulos, Yanyu Chen, and Lei Zuo. 3D printed architected hollow sphere foams with low-frequency phononic band gaps. *Additive Manufacturing*, 30:100842, dec 2019. ISSN 22148604. doi: 10.1016/j.addma.2019.100842.
- [17] Christina J. Naify, Chia-Ming Chang, Geoffrey McKnight, and Steven R. Nutt. Scaling of membrane-type locally resonant acoustic metamaterial arrays. *The Journal of the Acoustical Society of America*, 132(4):2784–2792, oct 2012. ISSN 0001-4966. doi: 10.1121/1.4744941.
- [18] D. Roca, O. Lloberas-Valls, J. Cante, and J. Oliver. A computational multiscale homogenization framework accounting for inertial effects: Application to acoustic metamaterials modelling. *Computer Methods in Applied Mechanics and Engineering*, 330:415–446, mar 2018. ISSN 00457825. doi: 10.1016/j.cma.2017.10.025.
- [19] D Roca, D Yago, J Cante, O Lloberas-Valls, and J Oliver. Computational design of locally resonant acoustic metamaterials. *Computer Methods in Applied Mechanics and Engineering*, 345:161–182, mar 2019. ISSN 00457825. doi: 10.1016/j.cma.2018.10.037.
- [20] D. Roca, T. Pàmies, J. Cante, O. Lloberas-Valls, and J. Oliver. Experimental and Numerical Assessment of Local Resonance Phenomena in 3D-Printed Acoustic Metamaterials. *Journal of Vibration and Acoustics*, 142(2):1–9, apr 2020. ISSN 1048-9002. doi: 10.1115/1.4045774.
- [21] Matthieu Rupin, Fabrice Lemoult, Geoffroy Lerosey, and Philippe Roux. Experimental Demonstration of Ordered and Disordered Multiresonant Metamaterials for Lamb Waves. *Physical Review Letters*, 112(23):234301, jun 2014. ISSN 0031-9007. doi: 10.1103/PhysRevLett.112.234301.
- [22] Ping Sheng, X.X. Zhang, Zhengyou Liu, and C.T. Chan. Locally resonant sonic materials. *Physica B: Condensed Matter*, 338(1-4):201–205, oct 2003. ISSN 09214526. doi: 10.1016/S0921-4526(03)00487-3.
- [23] Lucas Van Belle, Claus Claeys, Elke Deckers, and Wim Desmet. The impact of damping on the sound transmission loss of locally resonant metamaterial plates. *Journal of Sound and Vibration*, 461:114909, nov 2019. ISSN 0022460X. doi: 10.1016/j.jsv.2019.114909.
- [24] Viktor G. Veselago. The electrodynamics of substances with simultaneously negative values of ϵ and μ . *Soviet Physics Uspekhi*, 10(4):509–514, apr 1968. ISSN 0038-5670. doi: 10.1070/PU1968v010n04ABEH003699.
- [25] Eric C Wester, Xavier Brémaud, and Bryan Smith. Meta-Material Sound Insulation. *Building Acoustics*, 16(1):21–30, jan 2009. ISSN 1351-010X. doi: 10.1260/135101009788066555.
- [26] Yong Xiao, Jihong Wen, and Xisen Wen. Sound transmission loss of metamaterial-based thin plates with multiple subwavelength arrays of attached resonators. *Journal of Sound and Vibration*, 331(25):5408–5423, dec 2012. ISSN 0022460X. doi: 10.1016/j.jsv.2012.07.016.

- [27] Z. Yang, Jun Mei, Min Yang, N. H. Chan, and Ping Sheng. Membrane-Type Acoustic Metamaterial with Negative Dynamic Mass. *Physical Review Letters*, 101(20):204301, nov 2008. ISSN 0031-9007. doi: 10.1103/PhysRevLett.101.204301.
- [28] Z. Yang, H. M. Dai, N. H. Chan, G. C. Ma, and Ping Sheng. Acoustic metamaterial panels for sound attenuation in the 50–1000 Hz regime. *Applied Physics Letters*, 96(4):041906, jan 2010. ISSN 0003-6951. doi: 10.1063/1.3299007.
- [29] Hao-Jiang Zhao, Hong-Wei Guo, Ming-Xing Gao, Rong-Qiang Liu, and Zong-Quan Deng. Vibration band gaps in double-vibrator pillared phononic crystal plate. *Journal of Applied Physics*, 119(1):014903, jan 2016. ISSN 0021-8979. doi: 10.1063/1.4939484.
- [30] Xiaoling Zhou, Longqi Wang, Li Qin, and Fujun Peng. Improving sound insulation in low frequencies by multiple band-gaps in plate-type acoustic metamaterials. *Journal of Physics and Chemistry of Solids*, 146 (November 2019):109606, nov 2020. ISSN 00223697. doi: 10.1016/j.jpcs.2020.109606.